doi.org/10.26434/chemrxiv.9764774.v1

DFT and Thermodynamics Calculations of Surface Cation Release in LiCoO2

ali abbaspourtamijani, Joseph W. Bennett, Diamond T. Jones, Natalia Cartagena-Gonzalez, Zachary R. Jones, Elizabeth D. Laudadio, Robert Hamers, Juan A. Santana, Sara E. Mason

Submitted date: 03/09/2019 • Posted date: 06/09/2019

Citation information: abbaspourtamijani, ali; Bennett, Joseph W.; Jones, Diamond T.; Cartagena-Gonzalez, Natalia; Jones, Zachary R.; Laudadio, Elizabeth D.; et al. (2019): DFT and Thermodynamics Calculations of Surface Cation Release in LiCoO2. ChemRxiv. Preprint.

When exposed to environmental conditions, LCO can release Co cations, a known toxicant. In this study, we build on previous work (Bennett et al., Environ. Sci. Technol., 52, 5792-5802, 2018, Bennett et al., Inorg. Chem., 57, 13300-13311, 2018) using theory and modeling to understand the thermodynamic driving forces of ion release in water. We assess how the calculated predictions for ion release depend on aspects of the structural surface model. For example, we vary the number of atomic layers used to form the slab, we explore different surface terminations and hydroxyl group coverages, and we vary the periodic in-plane supercell to assess how ion release depends on the density of formed vacancies. We also benchmark the DFT + Thermodynamics modeling across a range of computational factors such as the choice of exchange correlation functional and pseudopotential type. Such assessment is critical, as there is no direct experimental information for comparison. We devise a generalizable scheme for predicting a threshold pH at which Co release from LCO becomes favorable. We put forward that this scheme could provide information about how much Co is released from LCO under variable pH conditions, and could therefore be used to inform macroscopic contaminant fate models.

File list (1)

DFT-and-Thermodynamincs-Surface-Cation-Release-LC... (1.86 MiB) view on ChemRxiv • download file

DFT and Thermodynamics Calculations of Surface Cation Release in $LiCoO_2$

Ali Abbaspour-Tamijani,[†] Joseph W. Bennett,[†] Diamond T. Jones,[†] Natalia Cartagena-Gonzalez,[‡] Zachary R. Jones,[¶] Elizabeth D. Laudadio,[¶] Robert J. Hamers,[¶] Juan A. Santana,[‡] and Sara E. Mason[*,†]

†*Department of Chemistry, University of Iowa, Iowa City, Iowa 52242*

‡*Department of Chemistry, The University of Puerto Rico at Cayey, P. O. Box 372230, Cayey, PR 00737-2230, USA*

¶*Department of Chemistry, University of Wisconsin-Madison, Madison, WI 53706*

E-mail: sara-mason@uiowa.edu

Abstract

While complex metal oxides (CMOs) such as $LiCoO_2$ (LCO) are currently used in multiple electronic devices, their environmental impacts are not well understood. In this work, we apply density functional theory (DFT) and thermodynamics modeling to study LCO surface transformations. We performed Raman studies on bulk LCO, and compared experimental and computational results. Full vibrational analysis of the model LCO surfaces show localized surface modes that are distinct from bulk, varying in Li and OH surface terminations. Owing to a lack of experimental information for surfaces, we carried out benchmarking studies in which model aspects and computational parameters are varied. Details of the cation release process are sensitive to the employed functional, and the results can be useful to establish upper- and lower-bounds for surface cation vacancy density under specified pH conditions. We found that surface Co dissolution beyond 22% in LCO may only occur at pH values that are chemically unreasonable, and that at pH close to 7, over 7% of surface Co will undergo dissolution. We go on to discuss how our results can provide useful insights to guide the (re)design of CMOs with controlled ion release.

Introduction

The production and widespread use of nanoscale complex metal oxides (CMOs) has been a driving force in the global economy,[1] specifically in the energy sector where Li-ion batteries[2–7] are the bedrock of portable electronics.[8,9] The prototypical electroactive CMO used in Li-ion batteries is $LiCoO_2$ (LCO), with production and use projected to increase.[10] With no established economic incentive to recycle LCO-based batteries,[11] they can contribute to electronic waste in landfills.[12] When exposed to different environmental conditions, CMO nanomaterials undergo transformations that are only beginning to be explored,[13–17] and which could have as-yet unknown biological impacts.[18–20] Therefore, molecular-level understanding of how CMOs transform outside of their operational settings and under variable envrionemntal conditions is critical. Furthermore, such information could be used to inform environmental release and fate models,[21–23] and to guide the design of environmentally benign nanomaterials. Such a scheme was recently applied in the case of binary metal oxide materials,[24,25] where high-throughput experimental works were used to inform hazard and risk profiles.

Recent experiments have demonstrated that CMOs such as LCO and $Li_x(Ni_yMn_zCo_{1-y-z})O_2$ (NMC)[17] will partially dissolve in aqueous media, releasing transition metals such as Co and Ni to solution. The metals released from these CMOs have shown toxicity effects in *Shewanella oneidensis* MR-1 bacteria,[10,16] the eukaryotic water flea *Daphnia magna*,[26] and have also been shown to potentially impact the lipid ordering in model cell membranes.[27,28] The mechanism for the release of metals from NMC has been studied with experimental and density functional theory (DFT) methods.[14,17] The results point to a multi-step release mechanism, where a surface exchange of Li and H takes place first, and subsequently the transition metals are released. The amount of released metals approximately increases in the order Li > Ni > Co > Mn. The results also indicate that the metal release mechanism is pH dependent and that the number of surface metal vacancies controls the thermodynamics and kinetics of the release process. For example, Billy *et al.* observed that NMC initially

released 33% of Ni, Mn, and Co.[17]

Building upon previous theoretical work of LCO surface stability,[13,29–31] here we apply DFT + Thermodynamics modeling to study cation release from the surface in aqueous environments. This comes after our studies of metal release from NMC and its compositionally tuned variants.[14,32] By focusing on the parent LCO material, we are able to assess model accuracy and go on to outline a general procedure to estimate the amount of surface metal that could dissolve from CMOs as a function of pH. Many of the surface properties calculated lack a direct experimental comparison. Therefore, we perform and reoprt on benchmarking studies in which computational and model parameters are varied. We also report Raman spectroscopy measurements of bulk LCO, and compare the results to the calculated spectrum. In going from the bulk to the surface, we identify surface-localized vibrational modes that differ from bulk modes, and which are also distinct between Li and OH terminated LCO surfaces.

Materials and Methods

Raman Spectroscopy

Raman studies were performed on commercial $LiCoO_2$ powder (MTI Corporation) on MgO substrates (MTI Corporation). Spectra were collected using a Thermo Fisher Scientific DXR Raman microscope using 532 nm excitation through a 10× objective. A full range grating (900 lines/mm) and a 25 μm slit width resulted in $\approx$2 cm^{-1} resolution. Spectra were adjusted to an atmospheric N_2 line at 2330 cm^{-1}.

DFT Calculations

DFT calculations were performed with Quantum Espresso[33] unless otherwise stated, using ultrasoft GBRV-type pseudopotentials.[34,35] Unless otherwise stated, calculations were carried out at the GGA-PBE + U level[36–42] with a Hubbard U value of 5.0 eV for the d-orbitals in

Co. A plane-wave cutoff of 40 Ry was used for the wavefunction, and 320 Ry for the charge density. During structural optimizations, all atoms were allowed to relax until forces were converged to less than 5 meV/Å. Calculations of vibrational modes were carried out by finite displacement methods with the Phonopy package,[43] using a displacement of 0.01 Å . Bulk calculations are carried out using a $\sqrt{3} \times \sqrt{3}R30^0$ unit cell, for which the total energy is converged using a 6×6×2 k-grid, and a 1×l unit cell, for which the total energies converged using an 8×8×8 k-grid.

we also performed DFT calculations with Projector Augmented Wave (PAW) potentials[44] as implemented in Vienna Ab-initio Simulation Package (VASP).[45] As DFT fails to fully capture long-range effects ,[46,47] we tested the meta-GGA functional, SCAN ,[48] as well as a van der Waals-corrected one; vdW-BEEF .[49] A wavefunction cutoff energy of 550 eV was used for calculations with PAW potentials. We focus on the SCAN and vdW-BEEF methods because they have been recently suggested as optimal alternatives to GGA + U for various types of materials .[50,51]

DFT + Thermodynamics Modeling

To study ion release from the LCO surface, DFT + Thermodynamics modeling was used as in our previous work.[14,32] In this method, the Gibbs free energy of ion release, ΔG, is modeled step-wise using both computational and experimental information. The partitioning of elementary reactions is done such that the first term, ΔG_1, is based entirely on DFT calculations, including zero-point energy corrections to the DFT energy.[13] The chemical equations for the ΔG_1 are presented in detail in the section 3.3 Co Release from $LiCoO_2(001)$. Following Rong and Kolpak,[52] the second term is defined as: $\Delta G_2 = \Delta G^0_{\mathrm{SHE}}$ - $n_e e U_{\mathrm{SHE}}$ - $2.303 n_{\mathrm{H^+}}$kT pH + kT ln a$(\mathrm{H}_x\mathrm{AO}_y)^{z-}$, where $\Delta G^0_{\mathrm{SHE}}$ is the free energy of formation at standard state relative to the standard hydrogen electrode (SHE), eU_{SHE} is the applied potential relative to SHE, and $a^{z-}_{H_xAO_y}$ is the concentration of the dissolved constituent ions (assumed to be 1×10^{-6} M, from previous experiments[10,16]). n_e and $n_{\mathrm{H^+}}$ are the number of

electrons and protons, respectively. At conditions of U_{SHE}=0, ΔG can be computed under variable pH values to simulate environmentally relevant dissolution conditions. Based on Pourbaix diagrams,[53] $Co^{2+}_{(aq)}$ is the dominant aqueous speciation of cobalt up until pH = 7. At pH > 7, $HCoO^{-1}_{2(aq)}$ becomes the preferred speciation, and computed values of ΔG would be shifted to reflect the change in speciation, as discussed previously.[14]

Results and Discussion

Characterization of Bulk $LiCoO_2$

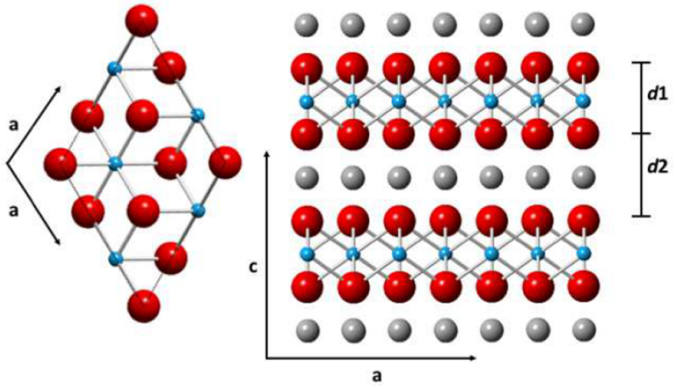

Figure 1: (Left) Top view of a transition metal oxide layer of the $\sqrt{3} \times \sqrt{3}R30^0$ bulk LCO cell. (Right) Side view of the layer ordering in LCO, with layer spacings $d1$ (O-Co-O) and $d2$ (O-Li-O). Co is depicted as cyan, Li is gray and O is red.

Figure 1 depicts a top view of bulk LCO (left-hand side), and a side view of the layered structure (right-hand side). Co resides in the center of an oxygen octahedra, and each octahedral unit is edge-sharing, forming a rigid O-Co-O network of height $d1$. Li is found in the space between O-Co-O units, which is of height $d2$. LCO belongs to the Delafossite structure type, so the overall crystal symmetry of the system is $R\bar{3}m$ (space group 166). In this structure, the Wyckoff positions are as follows: Li is at 3a, Co is 3b, and O is at 6c, with $u_O = 0.260$.

In Table 1 we report the lattice constants of bulk LCO, calculated with various DFT methods and experimental values. The DFT methods yield lattice constant values within

Table 1: Lattice parameters (Å) and band gap energy E_{gap} (eV) calculated with various DFT methods for bulk LCO. Experimental lattice parameters[54] and E_{gap} values[54–57] are also included.

DFTs	a	c	$d1$	$d2$	E_{gap}
GBRV-PBE+U5	2.843	14.120	2.065	2.643	2.59
PAW-PBE	2.847	14.009	2.029	2.640	1.02
PAW-PBE+U3.3	2.834	14.117	2.055	2.651	2.27
PAW-PBE+U5	2.828	14.177	2.073	2.653	2.84
PAW-SCAN	2.807	13.976	2.044	2.615	2.25
PAW-vdW-BEEF	2.858	14.017	2.061	2.612	1.16
Experiments	2.815	14.049	2.049	2.634	2.5-2.7

1.6 % of experimental values. As expected, as the applied U value is increased from 3.3 to 5.0 eV, there are increases in the inter-layer spacings and the c lattice constant. Overall, the SCAN functional results in the best agreement with experiment for the a lattice constant, which is in line with comparative studies assessing density functional performance in intercalating transition metal oxides.[50] The high accuracy of the SCAN functional for ground-state structures comes from the correct description of medium-range vdW interaction.[58] The most accurate c cell parameter is predicted by vdW-BEEF functional. This is due to the fact that this functional accounts for long-range effects, which play a role in interlayer interactions and distances. This role ultimately manifests in the value of the c lattice constant. We also included, in Table 1, calculated and measured values of the band gap energy, E_{gap}. The calculated values of E_{gap} for bulk LCO range from 1.02 to 2.8 eV in going from PBE to PBE + U with $U = 5$ eV, in line with previous calculations.[50,59,60] Interestingly, vdW-BEEF performs as poorly as PBE for E_{gap} of LCO, suggesting that such a method is unsuitable to study defected CMOs. This is likley because the type of the exchange functional used in the vdW-BEEF method is a revised PBE, which is only one parameter different than the PBE functionals. As such, it still carries the shortfalls of regular PBE functional in predicting E_{gap}. The experimental values for E_{gap} of LCO are 2.1,[55] 2.5[56] and 2.7[54,57] eV. The SCAN method also performs very well for the band gap of LCO as recently noted.[50] Note that our SCAN result for the band gap of LCO is 2.25 eV, while in Ref. 50 a value of 1.74 eV was

reported (see Table 2 in Ref. 50). However, inspection of the projected density of states (PDOS) in Fig. 3 of Ref. 50 reveals that the SCAN band gap for LCO is close to 2.4 eV. In general, calculations for LCO with PAW-PBE and GBRV-PBE yield similar structural and band gap properties.

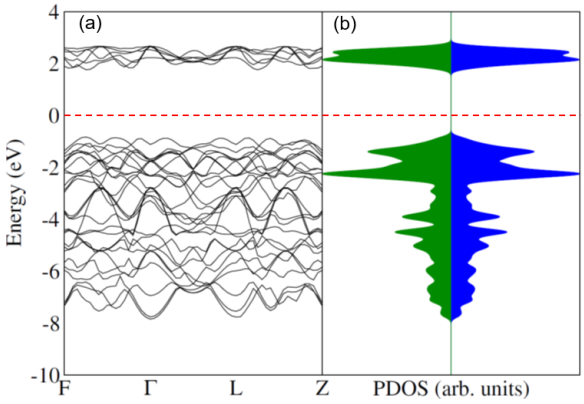

Figure 2: (a) Electronic band structure and (b) PDOS of bulk LCO calculated with the GBRV-PBE+U5 method. Spin-up and spin-down PDOS are shown in blue and green colors, respectively. The Fermi level (E_F) is shown as a dashed line set to E_F=0 eV.

DFT calculations were carried out for the electronic structure of the bulk LCO. Projected density of states (PDOS) and electronic band structure is shown in Figure 2. Analysis of the PDOS in Figure 2 shows an equal occupation of spin up and spin down $3d$ character, with more filled states than empty states; this is consistent with the $3d^6$ occupation formally associated with Co^{3+}. As the calculations with PAW potentials yield a similar electronic structure for bulk LCO, we only report the result from GBRV-PBE calculations, with an applied U value of 5.0 eV, referred to as GBRV-PBE+U5.

To further characterize the bulk structure, we performed an experimental Raman study and a computational vibrational analysis. The Raman spectrum of bulk LCO in the range 400 - 700 cm^{-1} is shown in Figure 3b. Two major peaks are observed, at 464.8 and 575.7 cm^{-1}. The DFT+U-calculated frequencies and normal modes of vibration for LCO are shown in Figure 3a. The doubly degenerate (xy-type) modes are shown on the left, and the singly degenerate (z-type) modes are shown on the right. Based on normal mode analysis, in general, the computed modes can be separated into three frequency regimes. The lower

frequency motions are Li-O based motions with some Co displacement mixed in, the middle frequency modes are Co-O based motions with some Li displacement mixed in, and the highest frequency modes are octahedral O_6 cage dilations.

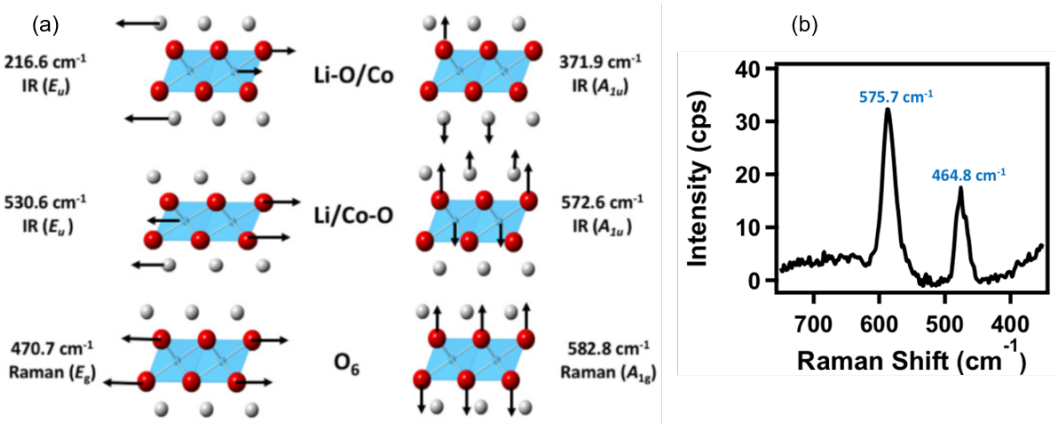

Figure 3: a) GBRV-PBE+U5 calculated vibrational modes and b) experimental Raman Spectra in the range of 400-700 cm^{-1} for bulk LCO.

The irreducible representations of the normal modes of LCO are $\Gamma = A_{1g} + E_g + 2A_{2u} + 2E_u$. The modes can be grouped as either IR ($2A_{2u}+2E_u$) or Raman ($A_{1g}+E_g$) active. The difference in frequency between the IR active modes in xy (E_u) and z (A_{2u}) for the Li-O/Co and Co-O/Li regimes are ≈ 155 and 42 cm^{-1}, so the two directions should be distinguishable in IR experiments. The Raman active modes from the DFT+U calculations are 470.7 and 582.8 cm^{-1}, close to the experimental values. The difference in frequency between the Raman active modes in xy (E_u) and z (A_{2u}) for the O_6 cage dilations is ≈ 112.1 cm^{-1}. Our calculated frequencies are in general agreement with a prior study of Li_xCoO_2, where the amount of Li was varied between x=0.33 and 0.87, and significant shifts in the A_{1g} and E_g were observed as the lithiation state was adjusted.[61]

$LiCoO_2$(001) Surfaces

Bulk LCO can be cleaved to expose (001), (104), and (110) surfaces,[62,63] with the polar (001) surface being predominant as shown by experiments[10,16] and DFT calculations.[29] Moreover, first-principles thermodynamics[13] show that the LCO(001) surface exhibits two distinct ter-

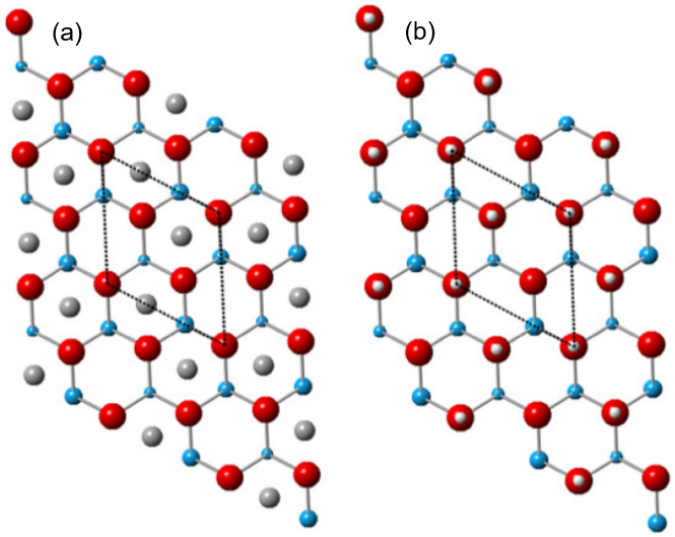

Figure 4: Top down view of the surface layer of LCO for (a) LCO_{h-Li} and (b) LCO_{h-H}. Li is on three-fold hollow surface sites and H is on-top surface oxygen-atoms, forming an O-H bond. The color scheme is the same as Figure 1.

minations as a function of chemical environment; *i*) a Li-terminated surface ($LCO(001)_{h-Li}$), where Li is above a three-fold hollow surface site (Figure 4a) and *ii*) an OH-terminated surface ($LCO(001)_{h-H}$), where H is directly above an O in the surface layer, forming an OH bond (Figure 4b). The previous calculations predict that the OH terminated surface is perferred under aqueous conditions.

In order to build structural models for the surface, two base unit cells were used. In one set, the surface slabs are based on the primitive hexagonal LCO bulk cell, which we use to create 1×1, 2×2, 3×2, 4×2, 5×2, 6×2, and 4×4 supercells. All surface slabs based on the hexagonal bulk cell include 3 O-Co-O trilayers. The second set of surface models is based on the $\sqrt{3} \times \sqrt{3}R30^0$ bulk LCO cell, and include $2\sqrt{3} \times \sqrt{3}$ and $3\sqrt{3} \times \sqrt{3}$ supercells comprised of 4 O-Co-O trilayers. Spanning these different surface models gives us the ability to study different vacancy densities formed upon removal of surface Co. For all supercell calculations, the *k*-grid is adjusted appropriately, such that the 1×1, 2×2, 3×2, 4×2, 5×2, 6×2, and 4×4 supercells uses *k*-grids of 8×8×1, 4×4×1, 3×4×1, 2×4×1, 2×4×1, 2×4×1, and 2×2×1, respectively. The $2\sqrt{3} \times \sqrt{3}$ and $3\sqrt{3} \times \sqrt{3}$ supercells use *k*-grids of 3×6×1 and 2×6×1, respectively.

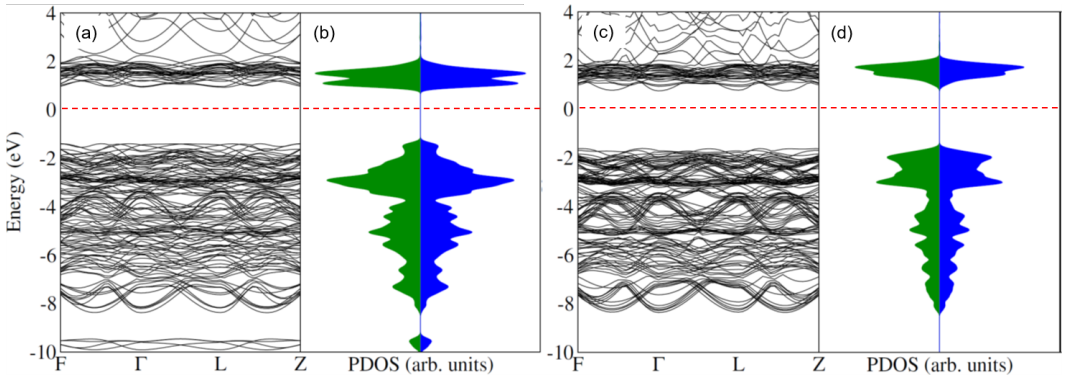

Figure 5: (a,c) Electronic band structure and (b,d) PDOS of (a,b) LCO(001)$_{\mathrm{h-H}}$ and (c,d) LCO(001)$_{\mathrm{h-Li}}$ calculated at the GBRV-PBE+U5 level. Color scheme is the same as Figure 2.

We discuss our DFT + U results for the electronic and vibrational properties of LCO(001)$_{\mathrm{h-Li}}$ and LCO(001)$_{\mathrm{h-H}}$ modeled with (2×2) supercell. The GBRV-PBE-U5 electronic band structure and PDOS of LCO(001)$_{\mathrm{h-Li}}$ and LCO(001)$_{\mathrm{h-H}}$ are shown in Figure 5. In Table 2, we include the E_{gap} of LCO(001)$_{\mathrm{h-Li}}$ and LCO(001)$_{\mathrm{h-H}}$ calculated with various DFT methods. In general, E_{gap} is similar for LCO(001)$_{\mathrm{h-Li}}$ and bulk LCO, with some variation between the various DFT methods. The value of E_{gap} is lower for LCO(001)$_{\mathrm{h-H}}$ than for LCO(001)$_{\mathrm{h-Li}}$, which results from an increase metallic character due to electron density delocalization on the surface of LCO(001)$_{\mathrm{h-H}}$ through the network of hydrogen bonding. The two LCO(001) surfaces, as well as bulk LCO, show similar PDOS profiles, pointing towards Co^{3+} as the oxidation state of Co at the surface.

Table 2: Values of the electronic band gap (eV) calculated with various DFT methods for LCO(001) and bulk LCO.

DFTs	LCO(001)$_{\mathrm{h-Li}}$	LCO(001)$_{\mathrm{h-H}}$	bulk LCO
GBRV-DFT+U5	2.37	2.33	2.59
PAW-PBE	1.10	0.87	1.02
PAW-PBE+U3.3	2.28	2.04	2.27
PAW-PBE+U5	2.77	2.57	2.84
PAW-SCAN	2.27	1.97	2.25
PAW-vdW-BEEF	1.06	0.95	1.16

The vibrational modes of the LCO(001) surfaces were calculated for comparison with the bulk vibrational modes. The normal modes of vibration for bulk LCO and bulk-like

vibrational modes of the two LCO(001) surface terminations are compared in Table 3. The largest shifts in frequencies are in the Co-O/Li (A_{1u}) and O_6 (A_{1g}) modes in the vertical direction. Relaxation of the two surfaces will change the $d1$ and $d2$ spacings, allowing for larger out of plane distortions than observed in-plane, when compared to the bulk structure. While the bulk-like vibrational modes of the two surfaces are shifted relative to the bulk, they should still be distinguishable.

Table 3: Vibrational frequencies (cm^{-1}) of the bulk-like vibrational modes in $LCO(001)_{h-Li}$ (Li-term) and $LCO(001)_{h-H}$ (OH-term). The frequency shift (cm^{-1}) of vibrations in the surface relative to bulk LCO are also included.

		bulk	Li-term	shift	OH-term	shift
Li-O/Co	E_u	216.6	213.2	-3.40	207.5	-9.10
Li-O/Co	A_{1u}	371.9	374.2	+2.30	372.0	-0.10
Co-O/Li	E_u	530.6	527.2	-3.40	528.4	-2.20
Co-O/Li	A_{1u}	572.6	555.4	-17.2	572.6	0
O_6	E_g	470.7	459.5	-11.2	462.0	-8.70
O_6	A_{1g}	582.8	594.8	+12.0	603.0	+20.2

There are distinct IR-active modes localized to the LCO surface. As shown in Figure 6, the Li and OH-terminated surfaces have surface mode frequencies that are discernible from each other. The surface Li IR active mode is at 386.7 cm^{-1}, and surface OH IR active mode is at 3576.2 cm^{-1}. We note that the Li-terminated surface localized mode is $\approx$ 15 cm^{-1} higher in frequency than the corresponding bulk motion and should be differentiable in experiment.

Co Release from $LiCoO_2(001)$

The initial dissolution of Co from LCO(001) is studied with a top-down model of metal release, and follows the preferred mechanism determined from previous work on (isostructural) NMC.[14] To summarize, we assume that the initial state is $LCO(001)_{h-Li}$, and that surface Li exchange with H to create $LCO(001)_{h-H}$. An HO-Co unit is then removed from $LCO(001)_{h-H}$. The surface exchange reaction is $LCO(001)_{h-Li}$ + x H $\rightarrow$ $LCO(001)_{h-H}$ + x Li, where dissolution of Li from LCO is an exothermic process. The chemical equation

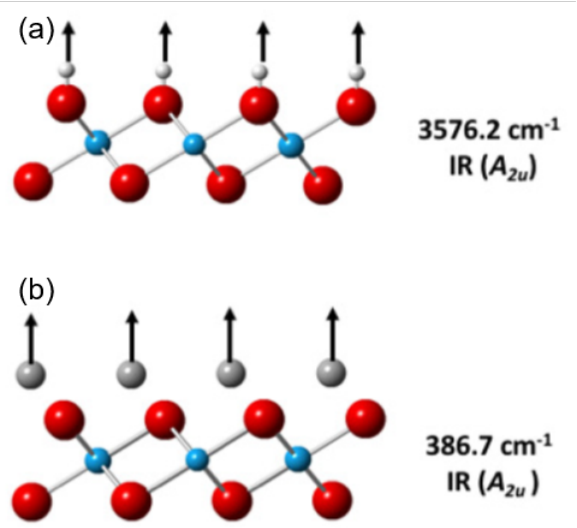

Figure 6: Calculated IR-active surface-localized vibrational modes of the (a) $LCO(001)_{h-H}$ and (b) $LCO(001)_{h-Li}$ surfaces.

for HO-Co release from LCO_{h-H} is: $LCO(001)_{h-H} \rightarrow LCO(001)_{vac} + Co_s + \frac{1}{2}H_{2,g} + \frac{1}{2}O_{2,g}$, where $LCO(001)_{vac}$ represents the slab structure that results from removal of a HO-Co unit from LCO_{h-H}. In the overall expression for $\Delta G = \Delta G_1 + \Delta G_2$, both the Li-H exchange and the subsequent OH-Co removal contribute to the ΔG_1 term, and each species (Co, H, O, Li) contributes to the ΔG_2 term, where the definition of ΔG_2 follows the details provided in the Materials and Methods, section 2.

ΔG_1 depends on multiple factors, including the details of the DFT calculations, the thickness of LCO(001) slab model, the surface hydroxyl group coverge, and the surface Co-vacancy density. We are able to computationally vary the Co-vacancy desntiy by using different surface supercells. We performed multiple calculations to isolate and study each of these effects. To explore how values of ΔG_1 depend on the DFT methods, we performed select calculations with GBRV-PBE+U5, PAW-PBE, PAW-PBE+U, PAW-SCAN and PAW-vdW-BEEF. The effects of the number of LCO layers was studied within GBRV-PBE+U5 and using a 2×2 surface model of $LCO(001)_{h-H}$ that included 3 O-Co-O layers and a $2\sqrt{3} \times \sqrt{3}$ surface model, which have an extra interior layer of O-Co-O. The effect of H-coverage in hydrogen-terminated LCO(001) was explored with a $3\sqrt{3}\times\sqrt{3}$ surface model with 55%, 44%

and 33% of H-coverage. We performed calculations with 2×2, 3×2, 4×2, 5×2, 6×2 and 4×4 surface models of LCO$(001)_{\mathrm{h-H}}$ to explore Co-vacancy density effects.

Table 4: ΔG_1 and ΔG (eV) calculated with various DFT methods for LCO(001).

DFTs	supercell	% H_{surf}	% Co_{vac}	ΔG_1	$\Delta G_{pH=3}$	$\Delta G_{pH=5}$	$\Delta G_{pH=7}$
PAW-PBE	5×2	50	10.00	13.22	-3.61	-3.25	-2.19
PAW-PBE+U3.3	5×2	50	10.00	15.21	-1.62	-1.27	-0.20
PAW-PBE+U5	5×2	50	10.00	14.89	-1.93	-1.58	-0.51
PAW-SCAN	5×2	50	10.00	17.20	0.37	0.73	1.79
PAW-vdW-BEEF	5×2	50	10.00	14.40	-2.43	-2.07	-1.01
GBRV-PBE+U5	5×2	50	10.00	15.46	-1.37	-0.66	0.05
GBRV-PBE+U5	3×2	50	16.67	12.16	1.77	2.25	2.72
GBRV-PBE+U5	$2\sqrt{3}\times\sqrt{3}$	50	16.67	11.49	1.10	1.57	2.04
GBRV-PBE+U5	$3\sqrt{3}\times\sqrt{3}$	55	11.11	14.04	-1.09	-0.38	0.33
GBRV-PBE+U5	$3\sqrt{3}\times\sqrt{3}$	44	11.11	14.89	-0.42	0.17	0.76
GBRV-PBE+U5	$3\sqrt{3}\times\sqrt{3}$	33	11.11	16.71	1.23	1.70	2.17

In Table 4 we present values of ΔG_1 and ΔG at various pHs and calculated with various DFT methods, using different surface models. By comapring ΔG_1 values for the 5×2 supercell, modeled using variable DFT computational parameters, we can assess how the energies depend on DFT methodology. Comparison shows that ΔG_1 values change by as much as 3.98 eV based on the details of the employed methods. This is not surprising given that ΔG_1 depends on the total energies of LCO slabs, Co_s, Li_s, $O_{2,g}$ and $H_{2,g}$, and none of the employed DFT methods consistently capture the properties of metallic, semi-conducting and molecular systems. Table 4 also shows how ΔG_1 and ΔG change with the number of LCO layers in the surface model; see GBRV-PBE-U5 calculations with the 3×2 (3 O-Co-O trilayer) and $2\sqrt{3}\times\sqrt{3}$ (4 O-Co-O trilayer) models. ΔG_1 decreases from 12.16 to 11.49 eV in going from 3 O-Co-O trilayers to 4 trilayers. These results relfect that slabs with more atomic layers are more stable, and thus less sensitive to vacancy formation. The results also show that our surface energetics calculated with 3 O-Co-O trilayer surface models of LCO(001) are upper-bounded values. For the $3\sqrt{3}\times\sqrt{3}$ LCO surface, the OH-surface coverage was changed from 5/9 to 4/9 and 3/9 to study how the extent of surface hydroxylation affects Co dissolution. Table 4 shows that for higher OH coverages, Co dissolution is more favorable,

and that below a threshold value of ≈ 40%, the process may not occur. The calculations yield insight into how the dissolution process will stop after time, which has been experimentally investigated across a wide range of Li-ion battery cathode material compositions based on LCO and related CMOs.[10,15,16]

Table 5: ΔG_1 and ΔG (eV) calculated with various DFT methods and surface Co-vacancy density for $\mathrm{LCO(001)_{h-H}}$.

DFT	supercell	% $\mathrm{H_{surf}}$	% $\mathrm{Co_{vac}}$	ΔG_1	$\Delta G_{\mathrm{pH=3}}$	$\Delta G_{\mathrm{pH=5}}$	$\Delta G_{\mathrm{pH=7}}$
PAW-PBE	2×2	50	25.00	8.23	1.06	1.24	1.77
PAW-PBE	4×2	50	12.50	11.70	-1.91	-1.61	-0.73
PAW-PBE+U3.3	2×2	50	25.00	9.92	2.74	2.92	3.45
PAW-PBE+U3.3	4×2	50	12.50	13.69	0.08	0.37	1.26
PAW-PBE+U5	2×2	50	25.00	9.16	1.98	2.16	2.69
PAW-PBE+U5	4×2	50	12.50	13.12	-0.49	-0.19	0.69
PAW-SCAN	2×2	50	25.00	11.30	4.12	4.30	4.83
PAW-SCAN	4×2	50	12.50	15.44	1.84	2.13	3.02
PAW-vdW-BEEF	2×2	50	25.00	8.72	1.55	1.73	2.26
PAW-vdW-BEEF	4×2	50	12.50	12.65	-0.96	-0.66	0.22
GBRV-PBE+U5	2×2	50	25.00	10.08	2.90	3.26	3.61
GBRV-PBE+U5	4×2	50	12.50	13.93	0.32	0.91	1.50
GBRV-PBE+U5	6×2	50	8.33	17.26	-2.79	-1.96	-1.13
GBRV-PBE+U5	4×4	50	6.25	20.49	-5.59	-4.53	-3.46

We now turn to discuss the effect of surface Co-vacancy density on ΔG_1 and ΔG . Table 5 shows ΔG_1 and ΔG values for Co vacancy densities ranging from 25% down to 6.25%. We discuss the results in terms of the the extrema. From Table 5, ΔG increases linearly with decreasing % Co vacancy. The linear relationship is driven by the surface exchange reaction $\mathrm{LCO(001)_{h-Li}} + x\ \mathrm{H} \rightarrow \mathrm{LCO(001)_{h-H}} + x\ \mathrm{Li}$. By calculating ΔG as a function of pH, we can fit ΔG as a function of pH, and determine the pH value at which ΔG=0. We consider this pH to be the calculated threshold for the onset of surface Co dissolution for a given Co vacancy density. The results of the threshold pH for variable Co vacancy denstiy, calculated with varous DFT methods, are plotted in Figure 7. Overall, surface Co dissolution beyond 22% may only occur at pH values that are chemically unreasonable. At conditions of pH close to 7, the model predicts that over 7% of surface Co will undergo dissolution. This interpretation correlates to recent studies in which low pH leaching processes were developed

to recycle metals from CMOs. Removal of Co from LCO required chelating and reducing agents, such as ascorbic acid and malic acid, to maximize leaching efficiency.[64–66] The trends presented here can also be related to the behavior of small molecule adsorbates such as phosphate[67] and carbonate, which have been shown to influence the dissolution of CMOs such as LCO and NMC.

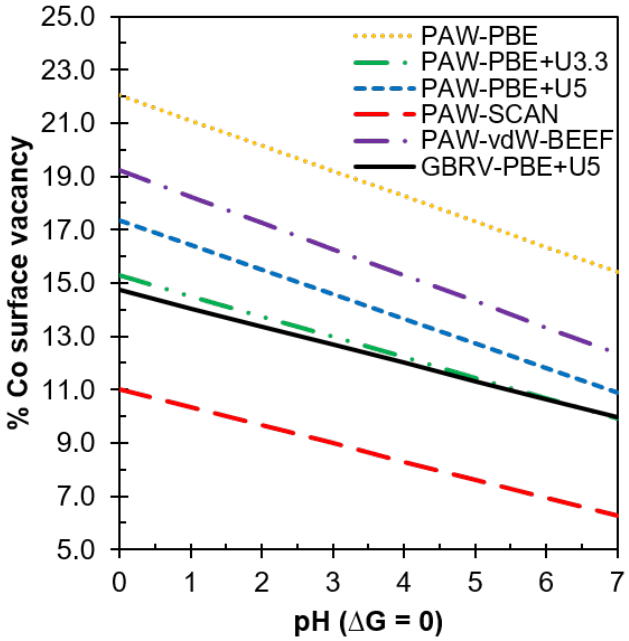

Figure 7: Co surface vacancy density (%) as a function of pH threshold (pH at which ΔG=0), calculated with various DFT methods.

We calculated the electronic band structure of LCO(001)$_{\text{vac}}$, the defect slab structure that results from Co release. As shown in Figure 8, after removal of a OH-Co surface group, E_{gap} decreases. Furthermore, the PDOS suggests that the oxidation state of surface Co in defected LCO(001) is Co^{4+}. The change in oxidation state is intuited based on the ideal $3d^5$ configuration of Co^{2+}, which exhibits unequal fillings of spin up and spin down d-states. The change in oxidation state is also consistent with standard operation of Li-ion batteries. The redox active transition metal (Co^{3+}) will respond to changes in the chemical environment (de-lithiation) by oxidizing.

We compare DFT results for the surface Co release in LCO and NMC, which are related by

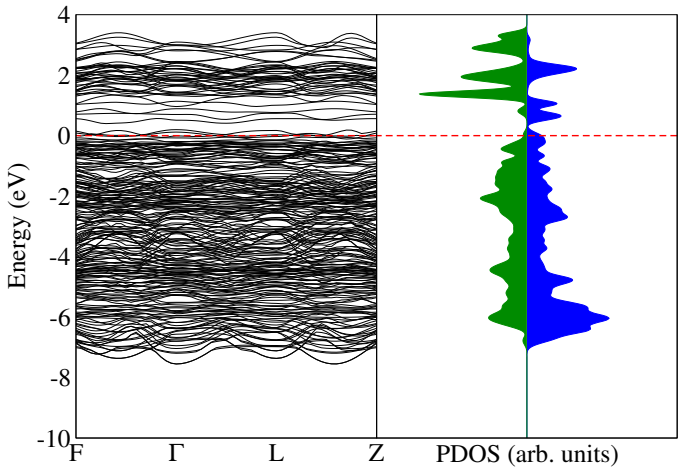

Figure 8: Electronic band structure (left) and PDOS (right) of $LCO(001)_{vac}$. Bands crossing E_F have Co $3d$ character as shown on the right panel.

compositional tuning. Calculations with the GBRV-PBE+U5 method shows that Co release from NMC is more favorable than from LCO at similar vacancy densities. For instance, ΔG at pH = 3 and 11.11 % Co vacancy is -0.44 eV in NMC, but predicted to be unfavorable in LCO. This may be explained in part by the differences in structural parameters, such as $d1$ and $d2$, which are 2.07Å and 2.64Å for LCO and 2.12Å and 2.62Å for NMC,[14] repsctively. $d1$ is the vertical O-Metal-O distance, and is 0.05Å larger in NMC than in LCO. This indicates that LCO forms stronger metal oxide bonds in the $d1$ layer than NMC. A more significant difference is found in the electronic structure of LCO and NMC; the addition of ferrimagnetic spin-coupling between Ni^{2+} (d^8) and Mn^{4+} (d^3), that results from the different oxidation states of the transition metal will destabilize the lattice relative to LCO, where Co^{3+} has a d^6 electron configuration and no net magnetic moment.

Conclusion

In the present work, we used Raman spectroscopy and DFT methods to study the properties of bulk $LiCoO_2$. Surface calculations assess how choices in structural models and employed DFT methods affect computed properties. We studied the dissolution process of LCO employing a DFT + Thermodynamics approach, spanning different surface super-

cells, OH coverage, slab thickness, and using different DFT methods. The results show that the DFT + Thermodynamics approach can be used to understand the interplay of surface transformations and metal release. The calculated surface Co dissolution energetics depends strongly upon surface area and environmental pH. We found that surface Co vacancy of LCO in water could be at least 7% at pH values close to 7. This information could be used to adjust environmental fate and toxicity models. The calculation results suggest that cation release processes can be controlled through fine-tuning the pH and other external chemical conditions. The ability to model cation release and the early stages of CMO dissolution could provide chemical guidance on future efforts to control release by design, and to guide CMO recycling strategies.

Author Information

Corresponding Author: sara-mason@uiowa.edu Notes: The authors declare no competing financial interest.

Acknowledgments

This work was supported by National Science Foundation Center for Chemical Innovation Program grant CHE-1503408 for the Center for Sustainable Nanotechnology. Specifically, A.A.T, J.W.B, D.T.J., Z.J., E.L., R.J.H and S.E.M. wish to acknowledge the Center for Chemical Innovation Program grant CHE-1503408 for the Center for Sustainable Nanotechnology. This research was supported in part through computational resources provided by The University of Iowa, Iowa City, Iowa and the National Science Foundation grant CHE-0840494. In particular, A.A.T., J.W.B., D.T.J. and S.E.M. wish to acknowledge computational resources provided by The University of Iowa, Iowa City, Iowa and the National Science Foundation grant CHE-0840494. This work used the Extreme Science and Engineering Discovery Environment (XSEDE67), which is supported by National Science Foundation grant

number ACI-1548562. A.A.T., J.W.B., D.T.J. and S.E.M. wish to acknowledge XSEDE resources provided by this grant. Computational resources were also provided in part by the High-Performance Computing Facility at the University of Puerto Rico, supported by an Institutional Development Award (IDeA) IN-BRE Grant Number P20GM103475 from the National Institute of General Medical Sciences (NIGMS), a component of the National Institutes of Health (NIH), and the Bioinformatics Research Core of the INBRE. N.C.G. and J.A.S. wish to aknowledge this grant. The contents are solely the responsibility of the authors and do not necessarily represent the ocial view of NIGMS or NIH. E. D. L. acknowledges support by National Science Foundation Graduate Research Fellowship under DGE-1256259. A.A.T., J.W.B., D.T.J. and S.E.M. thank Profs. Christy Haynes, Qiang Cui and Rigoberto Hernandez for useful discussions of this work.

References

(1) Keller, A. A.; McFerran, S.; Lazareva, A.; Suh, S. Global Life Cycle Releases of Engineered Nanomaterials. *J. Nanoparticle Res.* **2013**, *15*, 1692.

(2) Goodenough, J. B.; Kim, Y. Challenges for Rechargeable Li Batteries. *Chem. Mater.* **22**, *2010*, 587–603.

(3) Dunn, B.; Kamath, H.; Tarascon, J.-M. Electrical Energy Storage for the Grid: A Battery of Choices. *Science* **2011**, *334*, 928–935.

(4) Choi, N. S.; Chen, Z.; Freunberger, S. A.; Ji, X.; Sun, Y. K.; Amine, K.; Yushin, G.; Nazar, L. F.; Cho, J.; Bruce, P. G. Challenges Facing Lithium Batteries and ELectrical Double Layer Capacitors. *Angew. Chem. Int. Ed.* **2012**, *51*, 9994–10024.

(5) Goodenough, J. B.; Park, K.-S. The Li-Ion Rechargeable Battery: A Perspective. *J. Am. Chem. Soc.* **2013**, *135*, 1167–1176.

(6) Nitta, N.; Wu, F.; Lee, J.-T.; Yushin, G. Li-Ion Battery Materials: Present and Future. *Mater. Today* **2015**, *18*, 252–264.

(7) Jacoby, M. It's Time to get Serious about Recycling Lithium-Ion Batteries. *C&EN* **2019**, *97*, 1–3.

(8) Lu, J.; Chen, Z.; Ma, Z.; Pan, F.; Curtiss, L. A.; Amine, K. The Role of Nanotechnology in the Development of Battery Materials for Electric Vehicles. *Nature Nanotech.* **2016**, *11*, 1031–1038.

(9) Ellingsen, L. A.-W.; Hung, C. R.; Majeau-Bettez, G.; Singh, B.; Chen, Z.; Whittingham, M. S.; Stromman, A. H. Nanotechnology for Environmentally Sustainable Electromobility. *Nature Nanotech.* **2016**, *11*, 1039–1051.

(10) Hang, M. N.; Gunsolus, I. L.; Wayland, H.; Melby, E. S.; Mensch, A. C.; Hurley, K. R.; Pedersen, J. A.; Haynes, C. L.; Hamers, R. J. Impact of Nanoscale Lithium Nickel Manganese Cobalt Oxide (NMC) on the Bacterium *Shewanella oneidensis* MR-1. *Chem. Mater.* **2016**, 1092–1100.

(11) Dunn, J. B.; Gaines, L.; Kelly, J. C.; James, C.; Gallagher, K. G. The Significance of Li-Ion Batteries in Electric Vehicle Life-Cycle Energy and Emissions and Recycling's Role in its Reduction. *Energy Environ. Sci.* **2015**, *8*, 158–168.

(12) Zhang, K.; Schnoor, J. L.; Zeng, E. Y. E-Waste Recycling: Where Does It Go from Here? *Environ. Sci. Technol.* **2012**, *46*, 10861–10867.

(13) Huang, X.; Bennett, J. W.; Hang, M. N.; Laudadio, E. D.; Hamers, R. J.; Mason, S. E. *Ab initio* Atomistic Thermodynamics Study of the (001) Surface of $LiCoO_2$ in a Water Environment and Implications for Reactivity under Ambient Conditions. *J. Phys. Chem. C.* **2017**, *121*, 5069–5080.

(14) Bennett, J. W.; Jones, D.; Huang, X.; Hamers, R. J.; Mason, S. E. Dissolution of Complex Metal Oxides from First-Principles and thermodynamics: Cation Removal from the (001) Surface of $Li(Ni_{1/3}Mn_{1/3}Co_{1/3})O_2$. *Environ. Sci. Technol.* **2018**, *52*, 5792–5802.

(15) Gunsolus, I. L.; Hang, M. N.; Hudson-Smith, N. V.; Buchman, J. T.; Bennett, J. W.; Conroy, D.; Mason, S. E.; Hamers, R. J.; Haynes, C. L. Influence of Nickel Manganese Cobalt Oxide Nanoparticle Composition on Toxicity toward *Shewanella oneidensis* MR-1: Redesigning for Reduced Biological Impact. *Environ. Sci.: Nano.* **2017**, *4*, 636–646.

(16) Hang, M. N.; Hudson-Smith, N. V.; Clement, P. L.; Zhang, Y.; Wang, C.; Haynes, C. L.; Hamers, R. J. Influence of Nanoparticle Morphology on Ion Release and Biological Impact of Nickel Manganese Cobalt Oxide (NMC) Complex Oxide Nanomaterials. *ACS Appl. Nano Mater.* **2018**, *1*, 1721–1730.

(17) Billy, E.; Joulie, M.; Laucournet, R.; Boulineau, A.; Vito, E. D.; Meyer, D. Dissolution Mechanisms of $Li(Ni_{1/3}Mn_{1/3}Co_{1/3})O_2$ Positive Electrode Material from Lithium-Ion Batteries in Acid Solution. *ACS Appl. Mater. Interfaces* **2018**, *10*, 16424–16435.

(18) Maurer-Jones, M. A.; Gunsolus, I. L.; Murphy, C. J.; Haynes, C. L. Toxicity of Engineered Nanoparticles in the Environment. *Anal. Chem.* **2013**, *85*, 3036–3049.

(19) Lopez-Serrano, A.; Olivas, R. M.; Landaluze, J. S.; Camara, C. Nanoparticles: A Global Vision. Characterization, Separation, and Auantification Methods. Potential Environmental and Health Impact. *Anal. Chem.* **2014**, *6*, 38–56.

(20) Gunsolus, I. L.; Haynes, C. L. Analytical Aspects of Nanotoxicology. *Anal. Chem.* **2016**, *88*, 451–479.

(21) Gottschalk, F.; Sonderer, T.; nd B. Nowack, R. W. S. Modeled Environmental Concentrations of Engineered Nanomaterials. *Environ. Sci. Technol.* **2009**, *43*, 9216–9222.

(22) Weinberg, H.; Galyean, A.; Leopold, M. Evaluating Engineered Nanoparticles in Natural Waters. *Trends in Anal. Chem.* **2011**, *30*, 72–83.

(23) Westerhoff, P.; Nowack, B. Searching for Global Descriptors of Engineered Nanomaterial Fate and Transport in the Environment. *Acc. Chem. Res.* **2013**, *46*, 844–853.

(24) Nel, A.; and, T. X. Nanomaterial Toxicity Testing in the 21^{st} Century: Use of a Predictive Toxicological Approach and High-Throughput Screening. *Acct. Chem. Res.* **2013**, *46*, 607–619.

(25) Kaweeteerawat, C. et al. Toxicity of Metal Oxide Nanoparticles in *Escherichia coli* Correlates with Conduction Band and Hydration Energies. *Environ. Sci. Technol.* **2015**, *49*, 1105–1112.

(26) Bozich, J.; Hang, M.; Hamers, R. J.; Klaper, R. Core Chemistry Influences the Toxicity of Multicomponent Metal Oxide Nanomaterials, Lithium Nickel Manganese Cobalt Oxide, and Lithium Cobalt Oxide to *Daphnia magna*. *Environ. Toxicology and Chem.* **2017**, *36*, 2493–2502.

(27) Dogangun, M.; Hang, M. N.; Troiano, J. M.; McGeachy, A. C.; Melby, E. S.; Pedersen, J. A.; Hamers, R. J.; Geiger, F. M. Alteration of Membrane Compositional Asymmetry by $LiCoO_2$ Nanosheets. *ACS Nano* **2015**, *9*, 8755–8765.

(28) Dogangun, M.; Hang, M. N.; Machesky, J.; McGeachy, A. C.; Dalchand, N.; Hamers, R. J.; Geiger, F. M. Evidence for Considerable Metal Cation Concentrations from Lithium Intercalation Compounds in the Nano-Bio Interface Gap. *J. Phys. Chem. C.* **2017**, *121*, 27473–27482.

(29) Kramer, D.; Ceder, G. Tailoring the Morphology of $LiCoO_2$: A First Principles Study. *Chem. Mater.* **2009**, *21*, 3799–3809.

(30) Daheron, L.; Martinez, H.; Dedryvere, R.; Baraille, I.; Menetrier, M.; Denage, C.; Delmas, C.; Gonbeau, D. Surface Properties of $LiCoO_2$ Investigated by XPS Analyses and Theoretical Calculations. *J. Phys. Chem. C* **2009**, *113*, 5843–5852.

(31) Hu, L.; Xiong, Z.; Ouyang, C.; Shi, S.; Ji, Y.; Lei, M.; Wang, Z.; Li, H.; Huang, X.; Chen, L. *Ab initio* Studies on the Stability and Electronic Structure of $LiCoO_2$ (003) Surfaces. *Phys. Rev. B* **2005**, *71*, 125433–1–10.

(32) Bennett, J. W.; Jones, D.; Hamers, R. J.; Mason, S. E. A First-Principles and Thermodynamics Study of Compositionally-Tuned Complex Metal Oxides: Cation Release from the (001) Surface of Mn-rich Lithium Nickel Cobalt Oxide. *Inorg. Chem.* **2018**, *57*, 13300–13311.

(33) Giannozzi, P.; Baroni, S.; Bonini, N.; Calandra, M.; Car, R.; Cavazzoni, C.; Ceresoli, D.; Chiarotti, G. L.; Cococcioni, M.; Dabo, I.; et al., Quantum ESPRESSO: A Modular and Open-Source Software Project for Quantum Simulations of Materials. *J. Phys.: Condens. Matter* **2009**, *21*, 395502–20.

(34) Vanderbilt, D. Soft Self-Consistent Pseudopotentials in a Generalized Eigenvalue Formalism. *Phys. Rev. B Rapid Comm.* **1990**, *41*, 7892–5.

(35) Garrity, K. F.; Bennett, J. W.; Rabe, K. M.; Vanderbilt, D. Pseudopotentials for High-Throughput DFT Calculations. *Comp. Mater. Sci.* **2014**, *81*, 446–452.

(36) Hubbard, J. Electron Correlation in Narrow Energy Bands. *Proc. R. Soc. Lond. A* **1963**, *276*, 238–257.

(37) Anisimov, V. I.; Gunnarsson, O. Density-Functional Calculation of Effective Coulomb Interactions in Metals. *Phys. Rev. B.* **1991**, *43*, 7570.

(38) Anisimov, V. I.; Aryasetiawan, F.; Lichtenstein, A. I. First-principles Calculations of

the Electronic Structure of Strongly Correlated Systems: the LDA + U Method. *J. Phys. Cond. Matter* **1997**, *9*, 767.

(39) Shick, A. B.; Liechtenstein, A. I.; Pickett, W. E. Implementation of the LDA+U Method Using the Full-Potential Linearized Augmented Plane-Wave Basis. *Phys. Rev. B* **1999**, *60*, 10763–9.

(40) Cococcioni, M.; de Gironcoli, S. Linear Response Approach to the Calculation of the Effective Interaction Parameters in the LDA + U Method. *Phys. Rev. B* **2005**, *71*, 035105–1–16.

(41) Cococcioni, M. Accurate and Efficient Calculations on Strongly Correlated Minerals with the LDA + U Method: Review and Perspectives. *Rev. in Mineral. and Geochem.* **2010**, *71*, 147–167.

(42) Bennett, J. W.; Hudson, B. G.; Metz, I. K.; Liang, D.; Spurgeon, S.; Cui, Q.; Mason, S. E. A Systematic Determination of Hubbard U Using the GBRV Ultrasoft Pseudopotential Set. *Comp. Mater. Sci.* **2019**, *170*, 109137–1–10.

(43) Togo, A.; Tanaka, I. First-Principles Phonon Calculations in Materials Science. *Scripta Materialia* **2015**, *108*, 1–5.

(44) Kresse, G.; Joubert, D. From Ultrasoft Pseudopotentials to the Projector Augmented-Wave Method. *Phys. Rev. B* **1999**, *59*, 1758–1775.

(45) Kresse, G.; Furthmuller, J. Efficient Iterative Schemes for *Ab Initio* Total-energy Calculations Using a Plane-wave Basis Set. *Phys. Rev. B* **1996**, *54*, 11169–86.

(46) Aykol, M.; Kim, S.; Wolverton, C. van der Waals Interactions in Layered Lithium Cobalt Oxides. *J. Phys. Chem. C* **2015**, *119*, 19053–19058.

(47) Abbaspour Tamijani, A.; Salam, A.; de Lara-Castells, M. P. Adsorption of noble-gas

atoms on the TiO_2(110) Surface: An *ab initio*-assisted study with van der Waals-Corrected DFT. *J. Phys. Chem. C* **2016**, *120*, 18126–18139.

(48) Sun, J.; Ruzsinsky, A.; Perdew, J. P. Strongly Constrained and Appropriately Normed Semilocal Density FunctionalStrongly Constrained and Appropriately Normed Semilocal Density Functional. *Phys. Rev. Lett.* **2015**, *115*, 1–6.

(49) Wellendroff, J.; Lundgaard, K. T.; Mogelhoj, A.; Petzold, V.; Landis, D. D.; Norskon, J. K.; Bligaard, T.; Jacobsen, K. W. Density Functionals for Surface Science: Exchange-Correlation Model Development with Bayesian Error Estimation. *Phys. Rev. B* **2012**, *85*, 1–23.

(50) Chakraborty, A.; Dixit, M.; Aurbach, D.; Major, D. T. Predicting Accurate Cathode Properties of Layered Oxide Materials Using the SCAN Meta-GGA Density Functional. *Npj Computat. Mater.* **2018**, *4*, 1–9.

(51) Zheng, Y.; Zhang, M.; Li, Q.; Zhu, Y.; Sui, Z.; Chen, D. Electronic Origin of Oxygen Transport Behavior in La-Based Perovskites: A Density Functional Theory Study. *J. Phys. Chem. C* **2019**, *123*, 275–290.

(52) Rong, X.; Kolpak, A. M. Ab initio Approach for Prediction of Oxide Surface Structure, Stoichiometry, and Electrocatalytic Activity in Aqueous Solution. *Phys. Chem. Lett.* **2015**, *6*, 1785–1789.

(53) Persson, K. A.; Waldwick, B.; Lazic, P.; Ceder, G. Prediction of Solid-Aqueous Equilibria: Scheme to Combine First-Principles Calculations of Solids with Experimental Aqueous States. *Phys. Rev. B.* **2012**, *85*, 235438.

(54) van Elp, J.; Wieland, J. L.; Eskes, H.; Kuiper, P.; Sawatzky, G. A. Electronic Structure of CoO, Li-doped CoO, and $LiCoO_2$. *Phys. Rev. B* **1991**, *44*, 6090–6103.

(55) Kushida, K.; Kuriyama, K. Narrowing of the Co-3d band related to the Order–Disorder Phase Transition in $LiCoO_2$. *Solid State Commun.* **2002**, *123*, 349–352.

(56) Rosolen, J.; Decker, F. Photochemical Behavior of $LiCoO_2$ Membrane Electrode. *Electroanal. Chem.* **2001**, *501*, 253–259.

(57) Ensling, D.; Thissen, A.; Laubach, S.; Schmidt, P. C.; Jaegermann, W. Electronic Structure of $LiCoO_2$ Thin Films: A Combined Photoemission Spectroscopy and Density Functional Theory Study. *Phys. Rev. B* **2010**, *82*, 195431–1–16.

(58) J. H. Yang, D. A. K.; Ceder, G. Rationalizing Accurate Structure Prediction in the Meta-GGA SCAN Functional. *Phys. Rev. B* **2019**, *100*, 035132.

(59) Santana, J. A.; Jeongnim, K.; Kent, P. R. C.; Reboredo, F. A. Successes and Failures of Hubbard-Corrected Density Functional Theory: The Case of Mg Doped $LiCoO_2$. *J. Chem. Phys.* **2014**, *141*, 164706.

(60) van Elp, J.; Wieland, J. L.; Eskes, H.; Kuiper, P.; Sawatzky, G. A.; de Groot, F. M. F.; ; Turner, T. S. Calibrating Transition-Metal Energy Levels and Oxygen Bands in First-Principles Calculations: Accurate Prediction of Redox Potentials and Charge Transfer in Lithium Transition-Metal Oxides. *Phys. Rev. B* **2015**, *92*, 115118.

(61) Liu, H. L.; Ou-Yang, T. Y.; Tsai, H. H.; Lin, P. A.; Jeng, H. T.; Shu, G. J.; Chou, F. C. Electronic Structure and Lattice Dynamics of Li_xCoO_2 Single Crystals. *New J. Phys.* **2015**, *17*, 103004–1–8.

(62) Kim, Y.; Lee, H.; Kang, S. First-Principles and Experimental Investigation of the Morphology of Layer-Structured $LiNiO_2$ and $LiCoO_2$. *J. Mater. Chem.* **2012**, *22*, 12874–12881.

(63) Ohzuku, T.; Ueda, A. Solid-State Redox Reactions of $LiCoO_2$ $R\bar{3}m$ for 4 Volt Secondary Lithium Cells. *J. Electrochem. Soc.* **1994**, *141*, 2972–2977.

(64) Li, L.; Ge, J.; Chen, R.; Wu, F.; Chen, S.; Zhang, X. Environmental Friendly Leaching Reagent for Cobalt and Lithium Recovery from Spent Lithium-Ion Batteries. *Waste Management* **2010**, *30*, 2615–2621.

(65) Zeng, G.; Deng, X.; Luo, S.; Luo, X.; Zou, J. A Copper-Catalyzed Bioleaching Process for Enhancement of Cobalt Dissolution from Spent Lithium-Ion Batteries. *J. Hazard. Mater.* **2012**, *199-200*, 164–169.

(66) Li, L.; Lu, J.; Ren, Y.; Zhang, X. X.; Chen, R. J.; Wu, F.; Amine, K. Ascorbic-Acid-Assisted Recovery of Cobalt and Lithium from Spent Li-Ion Batteries. *J. Power Sources* **2012**, *218*, 21–27.

(67) Laudadio, E. D.; Bennett, J. W.; Mason, S. E.; Hamers, R. J. Impact of Phosphate Adsorption on Complex Cobalt Oxide Nanoparticle Dispersibility in Aqueous Media. *Environ Sci. Technol.* **2018**, *52*, 10186–10195.